Scientific Nexus

Vol 1(1) 2025:2276
https://doi.org/10.35472/scinexus.2276

RESEARCH ARTICLE

OPEN ACCESS

Sol-gel synthesis and characterization of iron-and nitrogen-doped titanium dioxide (TiO_2) photocatalysts for enhanced rhodamine B degradation

Ilma Maulidina[1], Dwi Febrianti[1], Priyan Prayogo[2], Rifqi Almusawi Rafsanjani[3], Iin Riananda[2], Ridho Hidayat[4], Laila Khafidatul Rosidah[1], Jesica Violina[1], Posman Manurung[5], Herman[6], Yayat Iman Supriyatna[7], Okta Ferli Suryadi[1], Indra Pardede[1,2*]

[1]Department of Physics, Faculty of Science, Sumatera Institute of Technology, 35365, Indonesia
[2]Department of Master Physics, Faculty of Science, Sumatera Institute of Technology, 35365, Indonesia
[3]Mathematic and Science Faculty, University of Indonesia, 16424, Indonesia
[4]Department of Chemistry, Sumatera Institute of Technology, 35365, Indonesia
[5]Department of Physics, University of Lampung, 3514, Indonesia
[6]Physics of Magnetic and Photonic Research Group division, FMIPA, ITB, Bandung, Indonesia
[7]National Research and Innovation Agency (BRIN) Iskandar Zulkarnain Tanjung Bintang, Tanjung Bintang, Indonesia
*Corresponding author: Jl Terusan Ryacudu, Way Hui, Jati Agung, South Lampung 35365, Indonesia. Email: indra.pardede@fi.itera.ac.id

ABSTRACT

Rhodamine B is a carcinogenic synthetic dye extensively used in textile and food industries, requiring effective removal from wastewater. Conventional titanium dioxide (TiO_2) photocatalysts demonstrate limited effectiveness under solar irradiation due to ultraviolet light activation requirements. This study evaluated strategic modification of TiO_2 electronic structure through low-concentration iron and nitrogen doping to enhance visible-light photocatalytic performance for rhodamine B degradation. Nanoscale TiO_2 materials were synthesized using sol-gel methodology and doped with iron and nitrogen precursors. Comprehensive characterization employed X-ray diffraction, ultraviolet-visible spectroscopy, and scanning electron microscopy to evaluate structural, optical, and morphological properties. Structural analysis confirmed preservation of anatase crystalline phase with 12.94 nanometer average crystallite size. Optical characterization revealed bandgap modifications from 3.27 eV for pure TiO_2 to 2.85 eV for iron-doped and 3.25 eV for nitrogen-doped samples. Nitrogen-doped TiO_2 achieved superior rhodamine B degradation efficiencies of 94.16% under ultraviolet irradiation and 83.34% under visible light, significantly outperforming pure and iron-doped materials. Enhanced performance resulted from optimized charge carrier dynamics balancing improved light harvesting with reduced electron-hole recombination. These findings establish a practical approach for developing cost-effective, solar-responsive photocatalysts for sustainable wastewater treatment applications.

Keywords: Bandgap engineering, nitrogen doping, photocatalytic degradation, rhodamine B degradation, sol-gel synthesis, titanium dioxide, wastewater treatment

PLAIN LANGUAGE SUMMARY

We developed an improved method to clean polluted water using sunlight. Industrial dyes like rhodamine B contaminate water and can cause cancer, making their removal critical for environmental safety. We modified titanium dioxide, a common cleaning material, by adding small amounts of iron or nitrogen to make it work better with visible light instead of just ultraviolet light. Our experiments showed that nitrogen-modified titanium dioxide performed exceptionally well, breaking down over 83% of the dye pollutant using ordinary sunlight. This offers a cost-effective, environmentally friendly solution for treating contaminated wastewater from textile and food industries, potentially reducing industrial pollution while utilizing renewable solar energy for water treatment applications.

Introduction

Rapid industrial development has significantly contributed to environmental pollution, particularly water contamination [1]. Industries such as textile, clothing, plastic, and paper manufacturing commonly use synthetic dyes in their production processes, generating wastewater with substantial environmental impacts [2].

Aquatic pollution from industrial dyes reduces the availability of clean water and damages aquatic ecosystems, affecting both fauna and flora [2]. These contaminants also pose serious health risks to humans, including carcinogenesis [3], anemia, and reduced blood platelet counts [4] when they enter the human body [5]. Therefore, effective treatment of dye-containing wastewater is crucial for environmental protection and public health.

Several methods have been developed for industrial wastewater treatment, including reverse osmosis, biological treatment, ozonation, adsorption, solid-phase filtration, oxidation, and coagulation

[6]. Among these approaches, oxidation methods demonstrate high efficiency in wastewater treatment by generating oxidizing species such as hydroxyl radicals (OH•), which can effectively degrade organic pollutants and inactivate microorganisms under light irradiation through photocatalytic processes.

Photocatalysis is a photoinduced reaction accelerated by the presence of a catalyst [7], enabling the degradation of organic pollutants into harmless compounds. This process can be classified into homogeneous and heterogeneous systems, with heterogeneous photocatalysis typically employing semiconductor materials as catalysts [8]. Semiconductors are characterized by electrical conductivity intermediate between conductors (e.g., copper) and insulators (e.g., glass), owing to their bandgap energy that separates the valence band from the conduction band [9].

Semiconductors used in photocatalysis are generally categorized into three groups: binary semiconductors (TiO_2, ZnO, Fe_2O_3, CdS, ZnS), ternary semiconductors ($SrZrO_3$, $PbCrO_4$, $CuInS_2$, Cu_2SnS_3), and quaternary semiconductors (Bi_2AlVO_7, Cu_2ZnSnS_4, $FeZn_2Cu_3O_{6.5}$) [7]. Among these materials, TiO_2 has emerged as one of the most extensively investigated semiconductor photocatalysts for organic contaminant removal due to its stable configuration and broad light spectrum activity, particularly under visible light [10].

TiO_2 is widely utilized as a photocatalyst because of its high thermal and chemical stability [11], excellent light absorption properties, non-toxicity, natural abundance, environmental compatibility, and relatively low cost [12]. Additionally, TiO_2 photocatalytic performance can be enhanced through various modifications, making it applicable in floating systems [13], responsive to visible light irradiation [14], and suitable for recyclable processes [15].

However, several factors limit the photocatalytic efficiency of TiO_2, including its wide bandgap [16], the influence of calcination temperature [17], rapid charge carrier recombination, and slow interfacial charge transfer [18]. TiO_2 exists in three crystal structures: rutile, anatase, and brookite. Among these phases, anatase exhibits the highest photocatalytic activity. Pure anatase-phase TiO_2 is a semiconductor with a bandgap of 3.2 eV, which limits its activation to UV light only [19].

Various strategies have been developed to enhance TiO_2 photocatalytic activity in the visible light range. These include doping with metal ions (Cu, Fe, V), non-metals (C, N) [20], and forming composites with materials such as SiO_2 [21]. Doping can modify the electronic structure around the Fermi level, thereby altering optical properties [22] and controlling semiconductor characteristics by introducing impurity atoms into the semiconductor surface [23].

The photocatalytic efficiency of TiO_2 depends on several critical parameters, including particle shape, size, crystal phase, crystallinity, and surface structure [23]. These properties are significantly influenced by the synthesis method employed. Various preparation methods have been used to obtain TiO_2 nanoparticles, including hydrothermal [24], solvothermal [25], sol-gel [26], direct oxidation, chemical vapor deposition (CVD) [27], electrodeposition, sonochemical, microemulsion, microwave, and precipitation methods.

Among these approaches, the sol-gel method offers several advantages, including simplicity, low cost, convenient process control, and the ability to mass-produce nanoparticles with large surface areas [28]. The sol-gel synthesis involves two key processes: hydrolysis and condensation of metal alkoxides, which eventually form metal oxides. This wet chemical method dissolves precursors in water or alcohol, converting them into gels through heating and stirring via hydrolysis/alcoholysis reactions. The resulting gel is then dried and calcined to achieve crystallinity and nano-sized particles [29].

This study aims to synthesize nano-sized titanium dioxide (TiO_2) using the sol-gel method and enhance its photocatalytic activity by modifying its optical properties, particularly the bandgap, through doping with metallic iron (Fe) and non-metallic nitrogen (N). Iron doping was selected for its ability to reduce bandgap energy and improve photocatalytic degradation by trapping photoexcited electrons and transferring them to O_2 molecules. This process promotes the separation of photogenerated electron-hole pairs, suppressing their recombination and enhancing overall photocatalytic activity [30].

Nitrogen doping contributes to bandgap narrowing and improves TiO_2 response under visible light, making it more effective for photocatalytic applications [31]. We hypothesize that Fe- and N-doped TiO_2 will exhibit superior photocatalytic performance under visible light irradiation compared to undoped TiO_2. The findings of this study are expected to contribute to the development of efficient photocatalysts for degrading organic compounds in wastewater, supporting efforts to mitigate water pollution caused by chemical contaminants.

Methods

Synthesis of TiO_2 catalyst

TiO_2 nanoparticles were synthesized via a modified sol-gel method adapted from previous research [1]. A total of 6 mL of titanium tetraisopropoxide (TTIP) was added to 25 mL of ethanol and stirred using a magnetic stirrer at 350 rpm for 150 minutes at room temperature. A separate solution consisting of 1 mL of HCl and 2 mL of distilled water was prepared concurrently. This HCl solution was then added dropwise every 15 minutes for 120 minutes. The pH of the solution was monitored throughout the process using a digital pH meter, maintaining a target pH range of 1.5-2.0. The resulting solution was allowed to stand for 24 hours at room temperature to facilitate complete gel formation. The gel was separated from the supernatant liquid and dried in an oven at 90°C for 60 minutes. The dried material was ground into fine powder using a mortar and pestle and subsequently calcined in a muffle furnace for 3 hours at 350°C.

Synthesis of Fe-doped TiO_2 (Fe:TiO_2)

Iron doping was performed using iron(II) sulfate heptahydrate ($FeSO_4{\cdot}7H_2O$) as the Fe source. Three solutions were prepared separately: (1) 6 mL of TTIP dissolved in 25 mL of ethanol, (2) 0.027 g of $FeSO_4{\cdot}7H_2O$ dissolved in 10 mL of distilled water, and (3) 1 mL of HCl mixed with 2 mL of distilled water. Solutions (1) and (2) were stirred separately at 350 rpm for 150 minutes at room temperature to ensure complete dissolution. Solution (2) containing the iron precursor was then slowly added to solution (1) over approximately 30 minutes while maintaining continuous stirring. Subsequently, solution (3) was added continuously dropwise over 120 minutes to initiate hydrolysis and condensation reactions. The pH was monitored and maintained within the range of 1.5-2.0 throughout the synthesis process. The solution was allowed to stand for 24 hours until complete gel formation occurred. The gel was then dried at 90°C for 60 minutes, ground using a mortar and pestle, and calcined at 350°C for 3 hours.

Synthesis of N-doped TiO_2 (N:TiO_2)

Nitrogen doping was carried out using urea (CH_4N_2O) as the nitrogen source. The synthesis procedure involved preparing three solutions: (1) 6 mL of TTIP dissolved in 25 mL of ethanol, (2) 0.006 g of CH_4N_2O dissolved in 10 mL of distilled water, and (3) 1 mL of HCl mixed with 2 mL of distilled water. Solutions (1) and (2) were stirred separately at 350 rpm for 150 minutes at room temperature. Solution (2) was slowly added to solution (1), followed by the dropwise addition of solution (3) every 15 minutes for 120 minutes. The pH was monitored using a digital pH meter and maintained between 1.5-2.0 during the synthesis. After pH stabilization, the solution was allowed to stand for 24 hours to achieve complete gel formation. The resulting gel was dried at 90°C for 60 minutes, ground into powder using a mortar and pestle, and calcined at 350°C for 3 hours.

Characterization

The synthesized samples were characterized using multiple analytical techniques to evaluate their structural, morphological, and optical properties. X-ray fluorescence (XRF) spectroscopy was employed to determine elemental composition and dopant concentration in the samples. X-ray diffraction (XRD) analysis was conducted using a diffractometer with Cu Kα radiation (λ = 1.5406 Å) operating at 40 kV and 30 mA to determine phase structure, crystallite size, and crystal quality. Diffraction patterns were recorded over a 2θ range of 10-80° with a step size of 0.02° and counting time of 1 second per step.

Ultraviolet-visible (UV-Vis) diffuse reflectance spectroscopy was applied to evaluate optical properties,

particularly bandgap energy determination. Spectra were recorded over a wavelength range of 200-800 nm using $BaSO_4$ as the reference standard. Bandgap energies were calculated using the Tauc plot method from the recorded reflectance data.

Scanning electron microscopy coupled with energy-dispersive X-ray spectroscopy (SEM-EDX) was utilized to examine microstructure, crystal morphology, and elemental distribution at the nanoscale. Samples were prepared by dispersing the powder on carbon-coated aluminum stubs and coating with a thin layer of gold to prevent charging effects during analysis.

Photocatalytic degradation test

The photocatalytic activity of the synthesized TiO_2, Fe-doped TiO_2 (Fe:TiO_2), and N-doped TiO_2 (N:TiO_2) catalysts was evaluated through the degradation of rhodamine B dye under both ultraviolet and visible light irradiation. A stock solution of rhodamine B was prepared at 100 ppm concentration using distilled water. For each photocatalytic experiment, 200 mL of this solution was transferred to a 250 mL glass beaker, and 0.1 g of the respective catalyst was added to achieve a catalyst loading of 0.5 g/L.

Prior to light exposure, the suspension was stirred in darkness for 30 minutes at 300 rpm to establish adsorption-desorption equilibrium between the dye molecules and catalyst surface. For UV light experiments, an OSRAM Ultra-Vitalux UV lamp (Model: Ultra-Vitalux 230V 300W) was used as the light source. This lamp operates at a rated power of 300 W and voltage of 230 V, emitting UV radiation in the range of 365–400 nm, with UVA output of 13.6 W and UVB output of 3 W. The lamp was positioned 30 cm above the reaction vessel to ensure uniform irradiation and safe thermal conditions. For visible light experiments, the setup was placed under natural sunlight conditions with an average light intensity of 800-1000 W/m^2 measured using a digital light meter.

During irradiation, the suspension was continuously stirred at 300 rpm and maintained at room temperature (25 ± 2°C). Aliquots of 10 mL were collected at predetermined time intervals of 0, 10, 20, 30, 40, 50, 60, 90, and 120 minutes. The collected samples were then left undisturbed overnight to allow settling of catalyst particles. The clear supernatant was subsequently analyzed using a UV-Vis spectrophotometer to monitor the concentration of rhodamine B.

The photocatalytic degradation efficiency was calculated using the following equation:

$$\text{Degradation efficiency (\%)} = [(C_0 - C)/C_0] \times 100$$

where C_0 represents the initial concentration of rhodamine B after dark adsorption equilibrium, and C represents the concentration at time t during the photocatalytic process. All experiments were conducted in triplicate to ensure reproducibility, and the results were reported as average values with standard deviations.

For kinetic analysis, the photocatalytic degradation was assumed to follow pseudo-first-order kinetics according to the Langmuir-Hinshelwood model:

$$-\ln(C/C_0) = kt$$

where k represents the apparent reaction rate constant (min^{-1}) and t is the irradiation time. The rate constants were determined from the slope of linear plots of $-\ln(C/C_0)$ versus time.

Results

Catalyst visualization

The sol-gel synthesis process involves two fundamental chemical reactions: hydrolysis and condensation. During hydrolysis, the titanium tetraisopropoxide (TTIP) precursor undergoes reaction with water molecules in the presence of ethanol as a solvent, leading to the formation of titanium hydroxide intermediates. The subsequent condensation process facilitates the development of three-dimensional sol networks for TiO_2, Fe:TiO_2, and N:TiO_2 nanomaterials. The aging process, conducted through controlled thermal treatment, removes residual solvents and organic impurities while promoting the crystallization of the desired titanium dioxide phases. The final products obtained through this synthesis approach are presented in Figure 1.

The physical characteristics and specifications of the synthesized TiO_2, Fe:TiO_2, and N:TiO_2 products are summarized in Table 1.

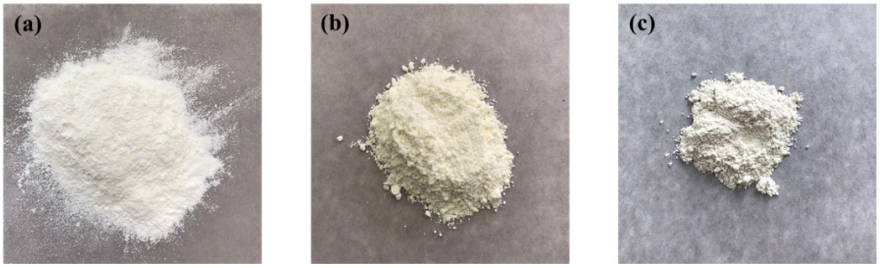

Figure 1. Physical appearance of synthesized photocatalytic materials. Visual documentation of sol-gel synthesized products showing (a) TiO_2 with characteristic white coloration, (b) Fe:TiO_2 displaying yellowish-white appearance, and (c) N:TiO_2 exhibiting grey coloration

Table 1. Physical specifications of synthesized TiO_2, Fe:TiO_2, and N:TiO_2 products

Classification	TiO_2	Fe:TiO_2	N:TiO_2
Color	White	Yellowish white	Grey
Weight	1.24 g	1.21 g	1.20 g
Smell	Odorless	Odorless	Odorless
Physical form	Powder	Powder	Powder
Crystal phase	Anatase	Not determined	Not determined

Table 2. Elemental composition determined by XRF analysis

Sample	TiO_2			Fe:TiO_2		N:TiO_2		
Element	Ti	Si	Fe	Ti	Fe	Ti	P	Cl
Concentration (%)	99.85	0.12	0.04	99.33	0.67	99.35	0.52	0.14

The pure TiO_2 sample exhibited the characteristic white coloration typical of anatase-phase titanium dioxide. Dopant incorporation resulted in distinct color changes that indicate successful modification of the electronic structure. The Fe-doped sample displayed a yellowish-white appearance, while the N-doped sample appeared grey. These color variations suggest the formation of intermediate energy levels within the TiO_2 bandgap structure, which can enhance visible-light absorption properties. All synthesized materials were obtained as fine powders without detectable odors, confirming their stability and the absence of volatile impurities. Minor weight variations among the samples, ranging from 1.20 g to 1.24 g, can be attributed to differences in dopant incorporation and particle formation kinetics during the sol-gel process. Only the pure TiO_2 sample was confirmed to be in the anatase phase based on preliminary characterization, because no XRD data for doped samples.

X-ray fluorescence analysis

X-ray fluorescence (XRF) spectroscopy was employed to determine the elemental composition and verify dopant incorporation in the synthesized materials. The quantitative analysis results are presented in Table 2.

The analysis revealed that pure TiO_2 contains predominantly titanium with trace amounts of silicon and iron (Fe), likely resulting from residual contamination during synthesis or sample preparation. The Fe:TiO_2 sample confirmed successful iron incorporation with a dopant concentration of 0.67%, demonstrating effective integration of iron species into the titanium dioxide matrix. The absence of nitrogen detection in the N:TiO_2 sample aligns with the inherent limitations of XRF spectroscopy for light elements with atomic numbers below 12 [32]. However, the presence of phosphorus (0.52%) and chlorine (0.14%) in this sample may originate from decomposition products of the urea nitrogen precursor or residual synthesis reagents.

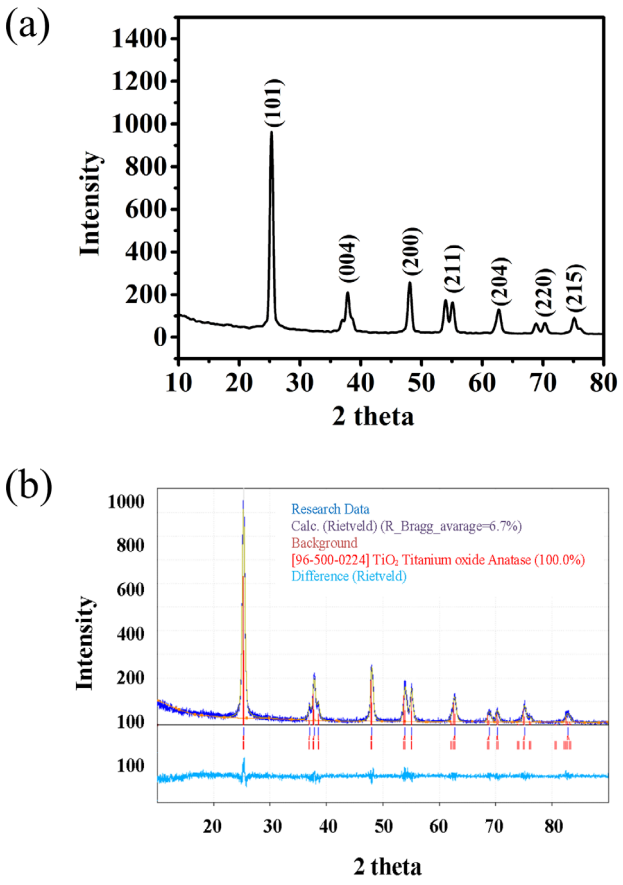

Figure 2. X-ray diffraction analysis and structural characterization of TiO_2 nanomaterial. (a) XRD diffraction pattern showing characteristic anatase phase peaks matching ICCD Card No. 21-1272, and (b) Rietveld refinement analysis using *Match!* software confirming tetragonal crystal structure with space group I41/amd and lattice parameters a = b = 3.7852 Å, c = 9.5057 Å. Average crystallite size determined as 12.94 nm using the Scherrer equation

X-Ray diffraction analysis

X-ray diffraction (XRD) analysis of the synthesized TiO_2 nanomaterial revealed characteristic diffraction peaks corresponding to crystal planes (101), (004), (200), (211), (204), (220), and (215) (Figure 2A). The diffraction pattern demonstrates excellent agreement with the standard reference for anatase-phase TiO_2 (ICCD Card No. 21-1272), confirming the predominant formation of the anatase crystal structure. The intentionally low doping concentrations (approximately 1%) employed in this study are generally insufficient to induce significant alterations in the primary crystal structure of TiO_2, according to established literature [30,31]. Therefore, the doped samples are expected to retain the anatase phase characteristics observed in the undoped material, making separate structural characterization of these variants unnecessary for the current investigation focused on photocatalytic performance enhancement.

Quantitative analysis of the crystallite size was carried out using the Scherrer equation:

$$D = \frac{K\lambda}{\beta cos\theta}$$

where D represents the average crystallite size, K is the shape factor (typically 0.9–1), λ is the X-ray wavelength, β denotes the full width at half maximum (FWHM) in radians, and θ is the Bragg diffraction angle. The calculated average crystallite size of the synthesized TiO_2 was determined to be 12.94 nm.

Rietveld refinement analysis was conducted to obtain more accurate structural parameters through least-squares minimization of differences between observed and calculated diffraction patterns. The refinement, performed using *Match!* software, yielded the results presented in Figure 2B. The excellent correspondence between observed and calculated patterns validates accurate phase identification and structural modeling. The refinement confirmed that the undoped TiO_2 sample crystallized in a tetragonal structure with space group I41/amd (No. 141) and lattice parameters of a = b = 3.7852 Å, and c = 9.5057 Å. The retention of the anatase phase in doped samples is anticipated based on the low dopant concentrations employed [33], although future comprehensive structural characterization will provide definitive confirmation of this assumption.

Scanning electron microscope and energy-dispersive spectroscopy X-Ray spectroscopy

Scanning electron microscopy examination of the synthesized TiO_2 sample revealed a heterogeneous surface morphology characterized by a broad distribution of grain sizes (Figure 3a). Particle size analysis confirmed the formation of nanostructured features with dimensions ranging from approximately 54 nm to 571 nm. The elemental mapping analysis demonstrates the spatial distribution of titanium and aluminum throughout the examined area (Figure 3b). The titanium distribution indicates the presence of TiO_2 particles, while the aluminum signal originates from the aluminum oxide substrate used during SEM analysis.

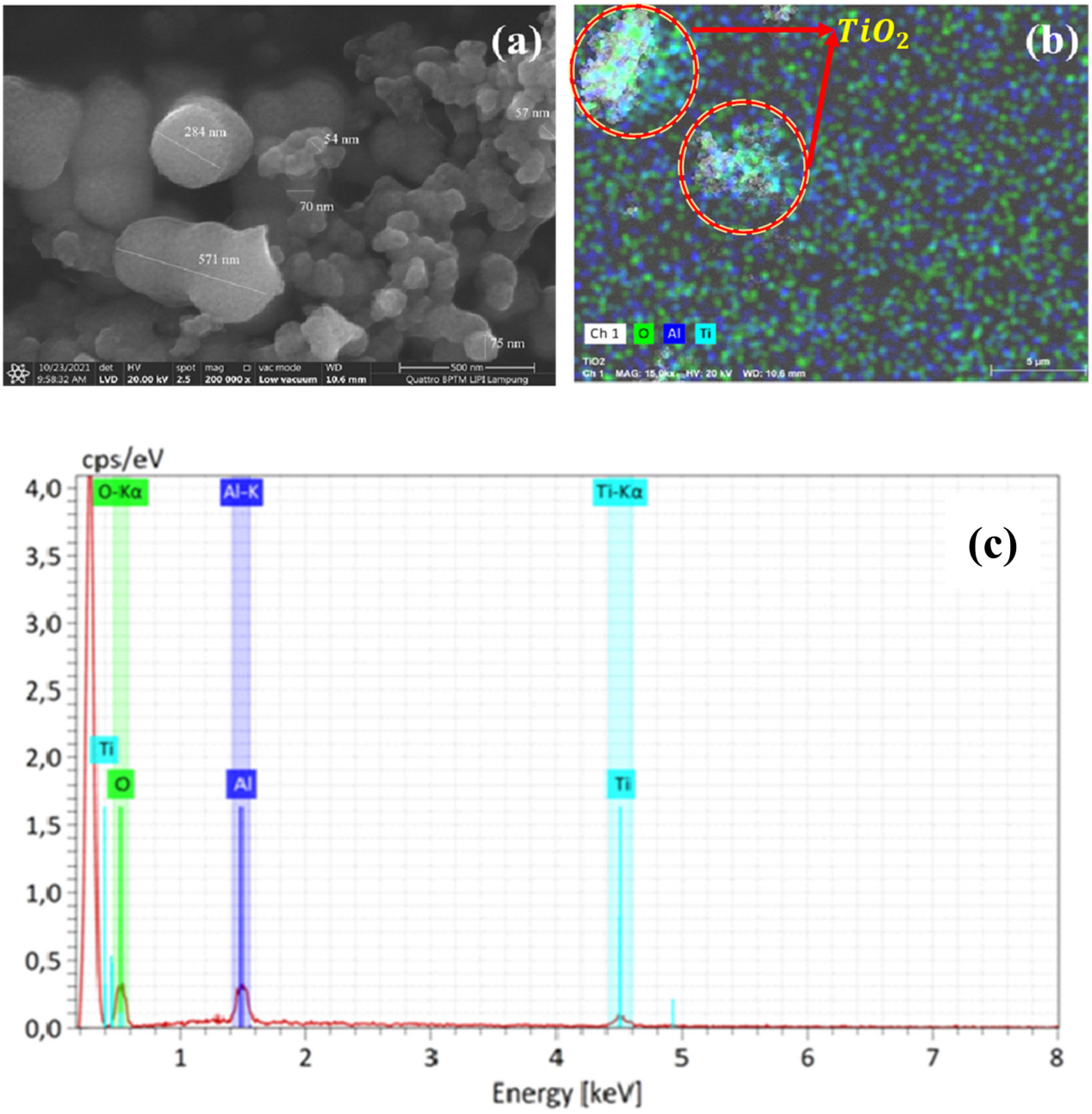

Figure 3. SEM-EDX characterization of TiO_2 nanomaterial. (a) Surface morphology showing heterogeneous grain distribution with particle sizes ranging from 54-571 nm, (b) elemental mapping analysis of titanium and aluminum distribution, (c) energy-dispersive X-ray spectrum revealing 83.15% oxygen, 5.66% titanium, and 11.20% aluminum. The aluminum content originates from the substrate, with approximately 34% of the surface area representing actual TiO_2 material

Energy-dispersive X-ray analysis revealed atomic percentages of 83.15% oxygen, 5.66% titanium, and 11.20% aluminum (Figure 3c). The substantial aluminum content and elevated oxygen concentration are attributed to the aluminum oxide sample holder employed during SEM-EDX observation. Based on the atomic ratio calculation of Ti/(Ti+Al), approximately 34% of the detected surface area consists of actual TiO_2 material, while the remainder represents contributions from the Al_2O_3 substrate. This substrate interference explains the apparent deviation from ideal TiO_2 stoichiometry in the quantitative analysis.

UV-Visible spectroscopy analysis

The optical absorption characteristics of synthesized TiO_2, Fe:TiO_2, and N:TiO_2 nanoparticles were investigated using UV-visible diffuse

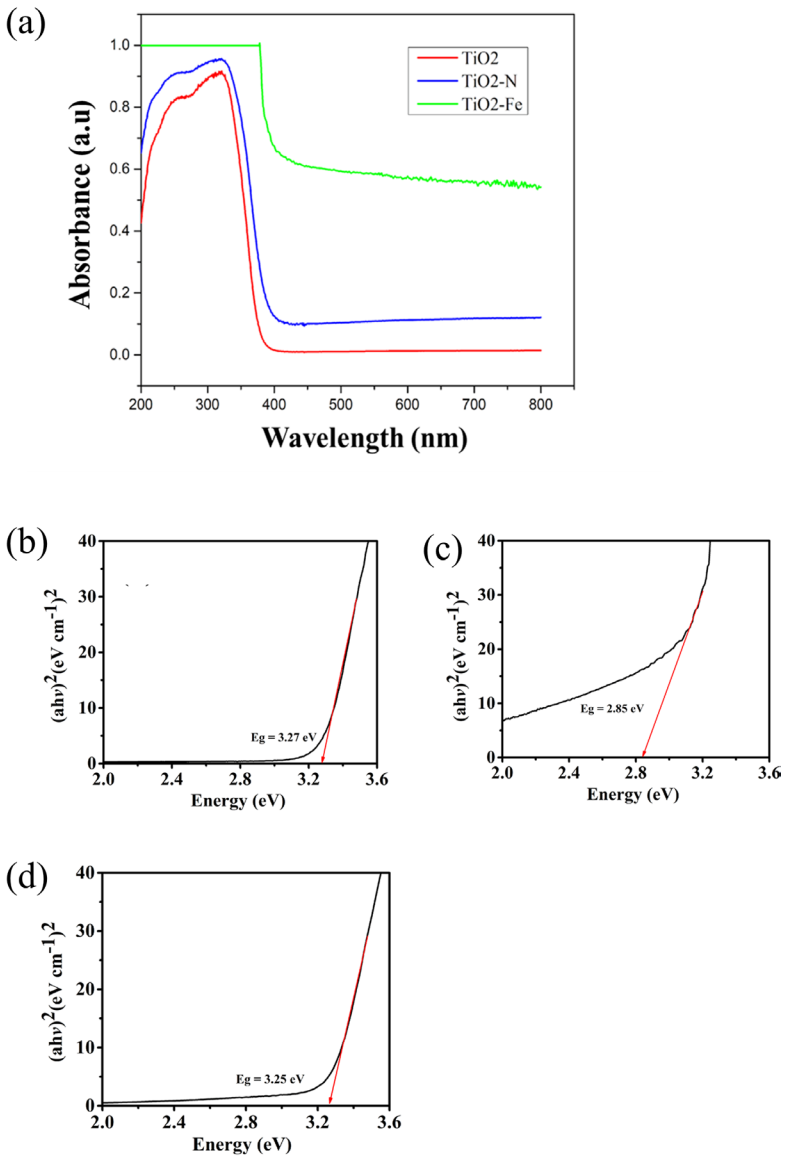

Figure 4. Optical characterization and bandgap analysis of synthesized photocatalysts. (a) UV-Vis absorption spectra of TiO_2, Fe:TiO_2, and N:TiO_2 nanoparticles, (b) Tauc plot analysis for bandgap energy determination of TiO_2, (c) Fe:TiO_2, (d) N:TiO_2 samples. The linear extrapolation method reveals bandgap energies of 3.27 eV, 2.85 eV, and 3.25 eV for TiO_2, Fe:TiO_2, and N:TiO_2, respectively

reflectance spectroscopy to evaluate the effects of dopant incorporation on electronic structure. Figure 4a presents the absorption spectra recorded over the wavelength range of 200-800 nm. The introduction of iron and nitrogen dopants into the TiO_2 lattice resulted in enhanced optical absorption intensity and induced red-shift behavior in the absorption edge, indicating extended absorption into longer wavelengths compared to undoped TiO_2.

The bandgap energies were determined through Tauc plot analysis [34], as shown in Figures 4b-d. The relationship between absorption coefficient and photon energy follows the equation (αhν)^(1/n) = A(hν - Eg), where α represents the absorption coefficient, hν is the photon energy, A is a constant, Eg is the bandgap energy, and n equals 2 for indirect transitions typical of TiO_2. Linear extrapolation of the Tauc plots to the energy axis yielded bandgap values of 3.27 eV for pure TiO_2, 2.85 eV for Fe:TiO_2, and 3.25 eV for N:TiO_2.

The observed bandgap narrowing is attributed to the creation of intermediate energy levels within the TiO_2 electronic structure. Iron doping introduces d-orbital states that form mid-gap levels, while nitrogen doping creates p-orbital states above the

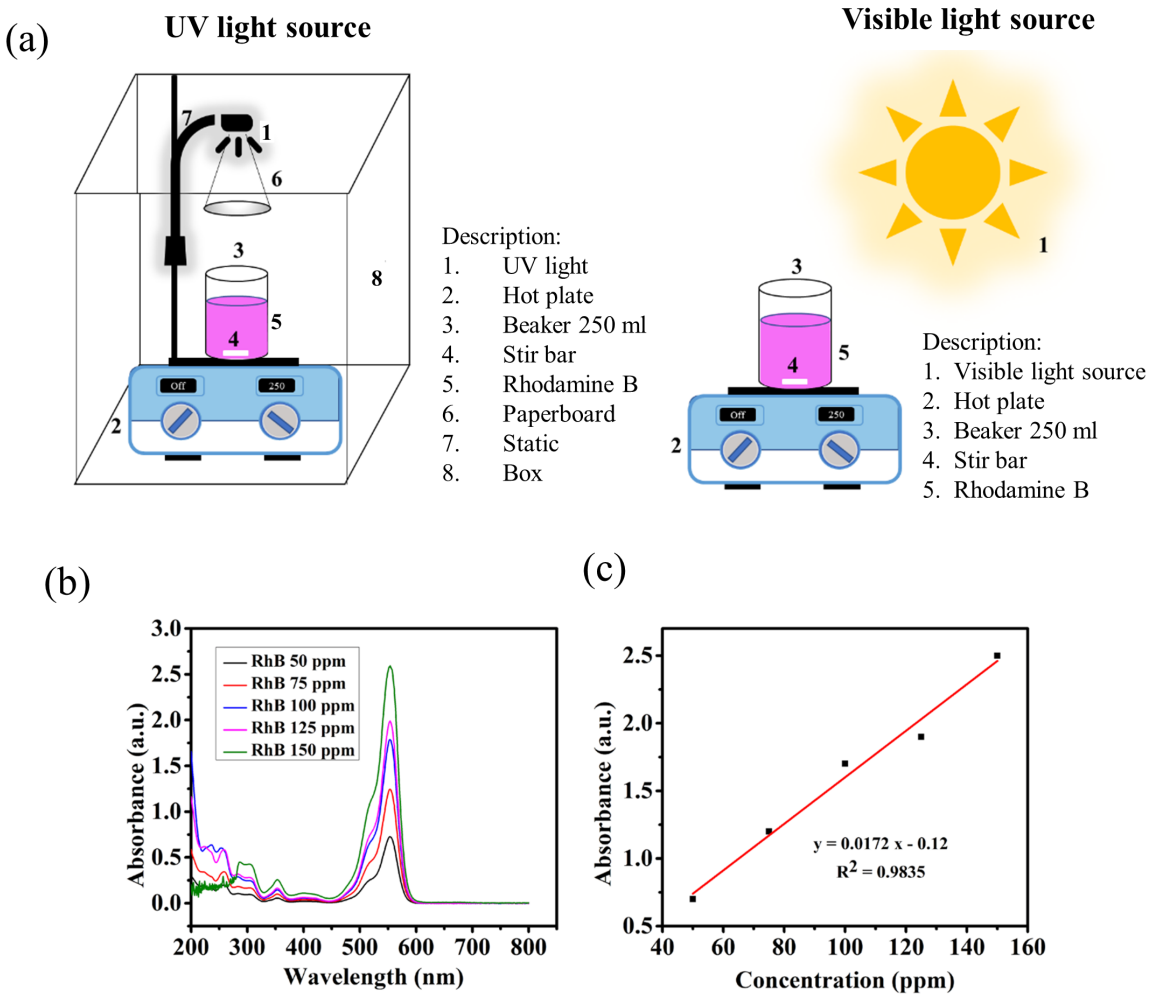

Figure 5. Experimental setup and analytical calibration for photocatalytic degradation assessment. (a) Photocatalytic test configuration under both UV and visible light irradiation conditions, (b) UV-Vis absorption spectra of rhodamine B solutions across different concentrations, (c) standard calibration curve establishing the linear relationship between rhodamine B concentration and absorbance with regression equation y = 0.0172x - 0.12 and correlation coefficient R^2 = 0.9835

valence band maximum. These modifications facilitate improved visible-light absorption and represent favorable conditions for enhanced photocatalytic activity under solar irradiation [30,35,36].

Photocatalytic degradation test

The photocatalytic activity of TiO_2, Fe:TiO_2, and N:TiO_2 was evaluated through rhodamine B degradation under both UV and visible light irradiation. The experimental protocol involved adding 0.1 g of catalyst to 200 mL of 100 ppm rhodamine B solution, followed by irradiation for 120 minutes with sample collection at predetermined intervals. Figure 5 illustrates the experimental setup and calibration procedures employed for quantitative analysis.

Standard rhodamine B solutions ranging from 50 to 150 ppm were analyzed to establish a reliable calibration relationship. Linear regression analysis yielded the equation y = 0.0172x - 0.12, where y represents absorbance and x denotes rhodamine B concentration in ppm. The high correlation coefficient (R^2 = 0.9835) confirms excellent adherence to Beer-Lambert law within the tested concentration range. The maximum absorption wavelength for rhodamine B was consistently observed at 550 nm throughout the photocatalytic experiments.

Based on the results, the maximum absorbance of rhodamine B before and after the photocatalytic process was consistently recorded at a wavelength of approximately 550 nm. This consistent peak allows reliable monitoring of rhodamine B degradation over time. Figure 6A presents the degradation profile of rhodamine B under UV light, while Figure 6B illustrates the degradation behavior under visible light. Visual inspection of the solutions before and

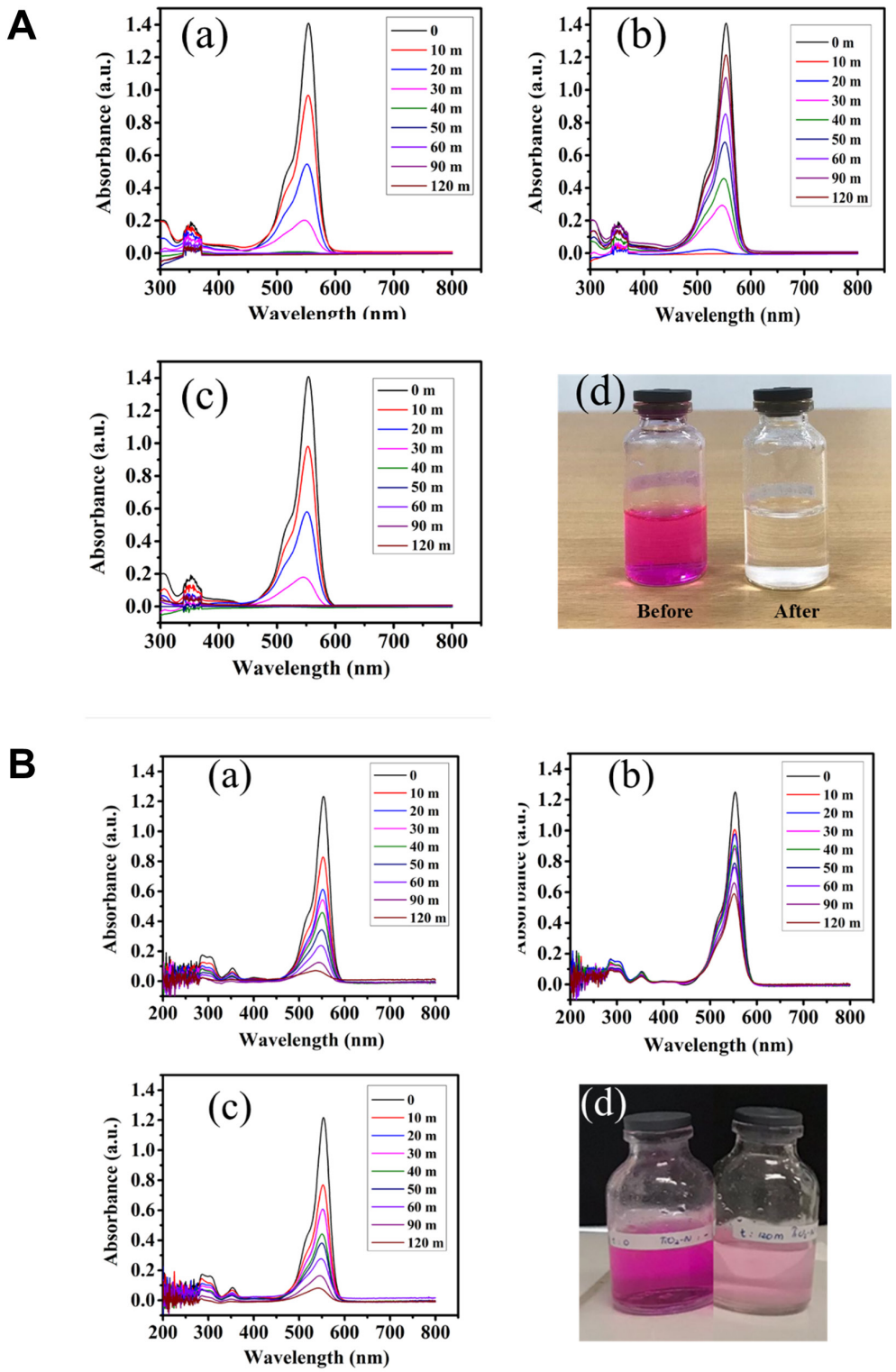

Figure 6. Photocatalytic degradation profiles of rhodamine B under different light conditions. Absorbance evolution during photocatalytic treatment under (A) UV light irradiation and (B) visible light irradiation using (a) TiO_2, (b) Fe:TiO_2, and (c) N:TiO_2 catalysts. The progressive decrease in absorbance at 550 nm demonstrates the effectiveness of each catalyst over the 120-minute treatment period. (d) Visual documentation of rhodamine B solution color changes from initial pink coloration to near-colorless final products confirms successful photocatalytic degradation across all tested systems

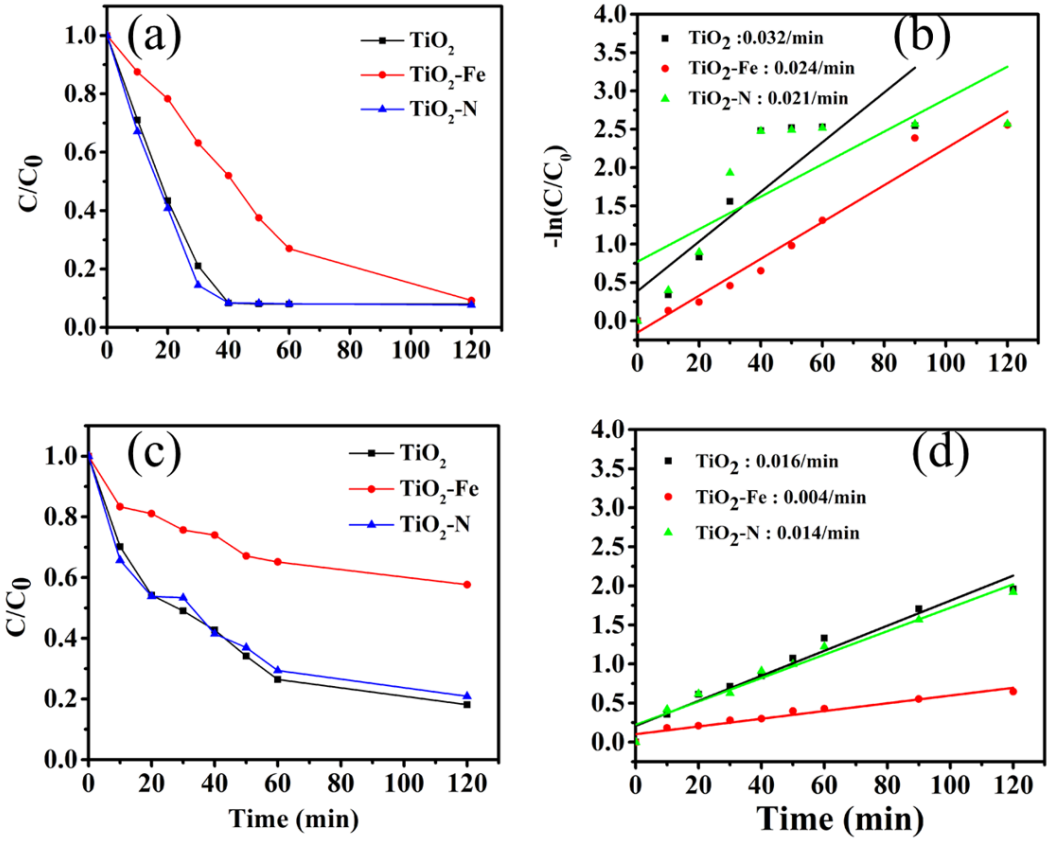

Figure 7. Kinetic analysis and degradation profiles of rhodamine B photocatalytic treatment. (a) Graph of rhodamine B concentration versus time under UV light irradiation, (b) Plot of $-ln(C/C_0)$ versus time illustrating the photocatalytic reaction kinetics under UV light, (c) Graph of rhodamine B concentration versus time under visible light irradiation, (d) Plot of $-ln(C/C_0)$ versus time illustrating the photocatalytic reaction kinetics under visible light

after treatment further confirms the degradation process through observable color changes from the characteristic pink rhodamine B solution to nearly colorless final products (Supplemental Figure 1). The results confirm that doping with Fe and N enhances TiO_2's ability to degrade organic pollutants under both UV and visible light irradiation.

Quantitative analysis of the photocatalytic results reveals distinct performance characteristics for each catalyst under different illumination conditions (Figure 7). The concentration profiles and kinetic analysis demonstrate that the degradation process follows pseudo-first-order kinetics according to the equation $-\ln(C/C_0) = kt$, where C_0 represents initial concentration, C is concentration at time t, and k is the apparent rate constant.

Under UV irradiation, the degradation efficiencies achieved after 120 minutes were 92.24% for TiO_2, 89.61% for Fe:TiO_2, and 94.16% for N:TiO_2. The corresponding apparent rate constants were 0.018, 0.015, and 0.021 min^{-1}, respectively. Under visible light exposure, the performance values reached 70.61% for TiO_2, 47.59% for Fe:TiO_2, and 83.34% for N:TiO_2, with rate constants of 0.014, 0.007, and 0.014 min^{-1}.

The results demonstrate that N:TiO_2 consistently exhibited superior photocatalytic performance under both illumination conditions, achieving the highest degradation efficiency and rate constant values. The enhanced performance is attributed to effective charge separation and reduced electron-hole recombination facilitated by nitrogen-induced electronic states. In contrast, Fe:TiO_2 showed reduced activity compared to pure TiO_2, particularly under visible light, despite its lower bandgap energy. This phenomenon suggests that iron-related defect states may function as recombination centers, offsetting the benefits of enhanced visible light absorption.

Discussion

This investigation examined the photocatalytic degradation of rhodamine B using pure TiO_2, Fe-doped TiO_2 (Fe:TiO_2), and N-doped TiO_2 (N:TiO_2) under both ultraviolet and visible light irradiations. A progressive decline in rhodamine B concentration, demonstrated by decreasing absorbance at 550 nm, confirmed effective photocatalytic activity across all tested materials. However, degradation efficiency varied depending on the type of dopant and the illumination source.

X-ray diffraction analysis established the predominant formation of the anatase phase in the synthesized TiO_2, which exhibits superior photocatalytic properties compared to alternative crystalline forms. While direct XRD characterization of the doped samples was not conducted, the low doping concentration (1%) employed in this study typically preserves the anatase crystal structure, as documented extensively in the literature [30,31]. This structural retention provides the foundation for the observed photocatalytic performance across all samples.

The reaction kinetics adhered to pseudo-first-order behavior, with N:TiO_2 exhibiting the highest apparent rate constant of 0.021 min^{-1}. This superior performance indicates enhanced charge separation and reduced electron-hole recombination, resulting from improved photon absorption characteristics and optimized electronic structure modifications.

Under ultraviolet light, all samples demonstrated effective photocatalytic degradation. N:TiO_2 achieved the highest degradation efficiency of 94.16% after 120 minutes, followed by TiO_2 (92.24%) and Fe:TiO_2 (89.61%). The reaction kinetics followed a pseudo-first-order model, with N:TiO_2 exhibiting the highest apparent rate constant of 0.021 min^{-1}. This superior performance indicates enhanced charge separation and reduced electron-hole recombination, resulting from improved photon absorption characteristics and optimized electronic structure modifications.

The transition to visible light illumination revealed distinct performance patterns. Fe:TiO_2 experienced a substantial decline in effectiveness, achieving only 47.59% degradation efficiency, while N:TiO_2 maintained strong performance at 83.34% and pure TiO_2 reached 70.61% after 120 minutes. Although Fe doping reduced the band gap energy, it did not translate into improved photocatalytic activity. This is likely due to increased charge carrier recombination, as previously reported by Linsebigler et al. (1995) [8], which offsets the benefits of enhanced visible light absorption.

UV-visible spectroscopy revealed that Fe:TiO_2 exhibited the lowest band gap energy (2.85 eV) compared to TiO_2 (3.27 eV) and N:TiO_2 (3.25 eV). While a narrower band gap generally favors visible-light absorption, excessive Fe-related mid-gap defect states may act as recombination centers, thereby diminishing photocatalytic efficiency.

X-ray fluorescence (XRF) analysis confirmed successful incorporation of Fe and N dopants into the TiO_2 matrix. Fe was detected at 0.67 wt% in Fe:TiO_2, while N was not directly detectable due to XRF's limitations in identifying light elements. Minor traces of phosphorus (P) and chlorine (Cl) were found in the N:TiO_2 sample, likely originating from precursor residues. The detectable Fe content correlated with band gap narrowing but did not contribute to improved degradation performance under visible light.

In contrast, N doping effectively enhanced photocatalytic activity under both light sources. The moderate band gap reduction to 3.25 eV enabled better solar light utilization while avoiding excessive charge recombination. This is reflected in the superior performance of N:TiO_2 in terms of both degradation efficiency and kinetic rate constants (k = 0.021 min^{-1} under UV and 0.014 min^{-1} under visible light).

These results emphasize that dopant selection critically influences the photocatalytic behavior of TiO_2. While both Fe and N altered the optical properties, only N doping provided a favorable balance between light absorption and charge carrier dynamics. Thus, N:TiO_2 represents a promising candidate for efficient photocatalytic degradation of organic pollutants like rhodamine B under both UV and visible light.

Conclusion

This study successfully demonstrated enhanced photocatalytic performance through strategic nitrogen doping of TiO_2, achieving superior degradation efficiency and reaction rate constants

under both ultraviolet and visible light conditions. Although Fe-doped TiO_2 exhibited the lowest band gap energy, its photocatalytic activity was limited, likely due to increased electron–hole recombination.

Characterization techniques including XRF and UV-Vis spectroscopy confirmed the successful incorporation of dopants and their respective impacts on the material's optical properties. Among the samples tested, N-doped TiO_2 demonstrated the most effective photocatalytic performance for rhodamine B degradation under both solar and UV light, indicating its potential for practical applications in wastewater treatment and environmental remediation.

Acknowledgment

The authors would like to express their gratitude to the Materials Physics Laboratory, Department of Physics, Institut Teknologi Sumatera (ITERA) for providing the facilities and technical support that enabled the completion of this research.

Declaration of interest

None.

Author contributions

Conceptualization: IM and IP; Methodology, IM and DF; Investigation and data analysis, IM and PP; Writing – original draft: IM; Writing – review & editing: IP, PP, and JV; Supervision and project administration: IP. All authors have read and agreed to the published version of the manuscript.

Received: June 30, 2025
Revised: July 9, 2025
Accepted: July 16, 2025
Published: July 28, 2025

References

1. Li Y, Lu L, Tan Y, Wang L, Shen M. Decoupling water consumption and environmental impact on textile industry by using water footprint method: A case study in China. Water. 2017;9(2):124. https://doi.org/10.3390/w9020124
2. Samchetshabam G, Choudhury TG, Gita S. Impact of textile dyes waste on aquatic environments and its treatment. Environment and Ecology. 2017, 35(3C): 2349-53.
3. Berradi M, Hajjaji N, Mohammedbenali A, Assoul M, Nounah A, El Harfi A. Textile finishing dyes and their impact on aquatic environs. Heliyon. 2019;5(11):e02711. https://doi.org/10.1016/j.heliyon.2019.e02711
4. Chowdhary P, Bharagava RN, Mishra S, Khan N. Role of industries in water scarcity and its adverse effects on environment and human health. In: Bharagava RN, editor. Environmental Concerns and Sustainable Development. Singapore: Springer; 2020:235–56. https://doi.org/10.1007/978-981-13-5889-0_12
5. Singh S, Parveen N, Gupta H. Adsorptive decontamination of rhodamine-B from water using banana peel powder: A biosorbent. Environ Technol Innov. 2018;12:189–95. https://doi.org/10.1016/j.eti.2018.09.001
6. Basavarajappa PS, Patil SB, Ganganagappa N, Reddy KR, Raghu AV, Reddy CV. Recent progress in metal-doped TiO_2, non-metal doped/co-doped TiO_2 and TiO_2 nanostructured hybrids for enhanced photocatalysis. Int J Hydrogen Energy. 2020;45(13):7764–78. https://doi.org/10.1016/j.ijhydene.2019.07.241
7. Ameta R, Ameta SC. Photocatalysis: Principles and Applications. Boca Raton: CRC Press; 2017.
8. Linsebigler AL, Lu G, Yates JT. Photocatalysis on TiO_2 surfaces: Principles, mechanisms, and selected results. Chem Rev. 1995;95(3):735–58. https://doi.org/10.1021/cr00035a013
9. Wang FF, Li Q, Xu DS. Recent progress in semiconductor-based nanocomposite photocatalysts for solar-to-chemical energy conversion. Adv Energy Mater. 2017;7(23):1700529. https://doi.org/10.1002/aenm.201700529
10. Kanan S, Moyet MA, Arthur RB, Patterson HH. Recent advances on TiO_2-based photocatalysts toward the degradation of pesticides and major organic pollutants from water bodies. Catal Rev Sci Eng. 2020;62(1):1–65. https://doi.org/10.1080/01614940.2019.1613323
11. Li ZJ, Yang H, Li B, Li L, Li W, Li Q, et al. Photoelectrochemically active and environmentally stable $CsPbBr_3/TiO_2$ core/shell nanocrystals. Adv Funct Mater. 2018;28(1):1704288. https://doi.org/10.1002/adfm.201704288
12. He X, Li X, Ma L, Zhao Q, Han D, He C, et al. Photocatalytic degradation of microcystin-LR by modified TiO_2 photocatalysis: A review. Sci Total Environ. 2020;743:140694. https://doi.org/10.1016/j.scitotenv.2020.140694
13. Xing Z, Zhang J, Cui J, Yin Y, Qiu P, Li Z. Recent advances in floating TiO_2-based photocatalysts for environmental application. Chemosphere. 2019;225:286–99. https://doi.org/10.1016/j.chemosphere.2019.03.033
14. Chen Y, Zheng Y, Wang H, Liu Y, Chen J, Wang S. Enhancement of photocatalytic performance with the use of noble-metal-decorated TiO_2 nanocrystals as highly active catalysts for aerobic oxidation under visible-light irradiation. Appl Catal B Environ. 2017;210:352–67. https://doi.org/10.1016/j.apcatb.2017.03.077

15. Kaur M, Sharma RK, Saini AK, Devi P, Mamba G, Mwakikunga B, et al. Marimo-bead-supported core–shell nanocomposites of titanium nitride and chromium-doped titanium dioxide as a highly efficient water-floatable green photocatalyst. ACS Appl Mater Interfaces. 2020;12(28):31327–39. https://doi.org/10.1021/acsami.0c07788

16. Katal R, Masudy-Panah S, Tanhaei M, Farahani MHDA, Jiangyong H. A review on the synthesis of the various types of anatase TiO_2 facets and their applications for photocatalysis. Chem Eng J. 2020;384:123384. https://doi.org/10.1016/j.cej.2019.123384

17. Aristanti Y, Supriyatna YI, Masduki NP, Soepriyanto S. Effect of calcination temperature on the characteristics of TiO_2 synthesized from ilmenite and its applications for photocatalysis. IOP Conf Ser Mater Sci Eng. 2019;478(1):012019. https://doi.org/10.1088/1757-899X/478/1/012019

18. Fonseca-Cervantes OR, Pérez-Larios A, Romero Arellano VH, Sulbaran-Rangel B, González CAG. Effects in band gap for photocatalysis in TiO_2 support by adding gold and ruthenium. Processes. 2020;8(9):1032. https://doi.org/10.3390/pr8091032

19. Nagaraj G, Irudayaraj A, Josephine RL. Tuning the optical band gap of pure TiO_2 via photon induced method. Optik. 2019;179:889–94. https://doi.org/10.1016/j.ijleo.2018.11.009

20. Ghorbanpour M, Feizi A. Iron-doped TiO_2 catalysts with photocatalytic activity. J Water Environ Nanotechnol. 2019;4(1):60–6. https://doi.org/10.22090/jwent.2019.01.006

21. Manurung P, Situmeang R, Ginting E, Pardede I. Synthesis and characterization of titania-rice husk silica composites as photocatalyst. Indones J Chem. 2015;15(1):36–42. https://doi.org/10.22146/ijc.21221

22. Zhao FA, Xiao HY, Bai XM, Zu XT. Effects of Ag doping on the electronic and optical properties of CdSe quantum dots. Phys Chem Chem Phys. 2019;21(29):16108–19. https://doi.org/10.1039/c9cp02433f

23. Al-Omary SS, Algharagholy LA, Al-Dokheily ME. Band gap modification of TiO_2 using solid state reaction with hydrides in argon atmosphere. Int J Eng Technol. 2018;7(4.36):354–7. https://doi.org/10.14419/ijet.v7i4.36.23804

24. Vijayalakshmi R, Rajendran V. Synthesis and characterization of nano-TiO_2 via different methods. Sch Res Libr. 2012;4(2):1183–90.

25. Ramakrishnan VM, Natarajan M, Santhanam A, Asokan V, Velauthapillai D. Size controlled synthesis of TiO_2 nanoparticles by modified solvothermal method towards effective photocatalytic and photovoltaic applications. Mater Res Bull. 2018;97:351–60. https://doi.org/10.1016/j.materresbull.2017.09.017

26. Dubey RS, Krishnamurthy KV, Singh S. Experimental studies of TiO_2 nanoparticles synthesized by sol–gel and solvothermal routes for DSSCs application. Results Phys. 2019;14:102390. https://doi.org/10.1016/j.rinp.2019.102390

27. Kumar A. Different methods used for the synthesis of TiO_2 based nanomaterials: A review. Am J Nano Res Appl. 2018;6(1):1–9. https://doi.org/10.11648/j.nano.20180601.11

28. Lukong VT, Ukoba KO, Jen TC. Heat-assisted sol–gel synthesis of TiO_2 nanoparticles: Structural, morphological and optical analysis for self-cleaning application. J King Saud Univ Sci. 2022;34(1):101746. https://doi.org/10.1016/j.jksus.2021.101746

29. Danks AE., Hall SR., Schnepp Z. The evolution of 'sol–gel' chemistry as a technique for materials synthesis. Mater. Horiz., 2016,3, 91-112. https://doi.org/10.1039/C5MH00260E

30. Ali T, Tripathi P, Azam A, Raza W, Ahmed AS, Ahmed A, Muneer M. Photocatalytic performance of Fe-doped TiO_2 nanoparticles under visible-light irradiation. Mater Res Express. 2017;4(1):015022. https://doi.org/10.1088/2053-1591/aa576d

31. Khan TT, Bari GAKMR, Kang HJ, Lee TG, Park JW, Hwang HJ, et al. Synthesis of N-doped TiO_2 for efficient photocatalytic degradation of atmospheric NOx. Catalysts. 2021;11(1):109. https://doi.org/10.3390/catal11010109

32. Orsilli J, Galli A. Angle-dependent XRF analyses: Pros and cons of a novel technique in the field of cultural heritage. Sustainability. 2024;16(4):1460. https://doi.org/10.3390/su16041460

33. Fujishima A, Zhang X, Tryk DA. TiO_2 photocatalysis and related surface phenomena. Surf Sci Rep. 2008;63(12):515–82. https://doi.org/10.1016/j.surfrep.2008.10.001

34. Shyniya CR, Bhabu KA, Rajasekaran TR. Enhanced electrochemical behavior of novel acceptor doped titanium dioxide catalysts for photocatalytic applications. J Mater Sci Mater Electron. 2017. https://doi.org/10.1007/s10854-017-6396-6

35. Rahman MA, Mahmud S, Uddin MJ, Rana M, Khan MN, Mia MAH. Synthesis, characterization and enhanced photocatalytic activity of nitrogen and fluorine co-doped TiO_2 under visible light irradiation. Chemical Papers. 2023;77(11):6129–6143. https://doi.org/10.1007/s11696-023-03078-7

36. Sadiq MM, Aziz SAA, Halin IA, Sabri MFM, Fazry S, Saravanan S, et al. Enhancement of photocatalytic activity of iron–nickel nanoparticle-doped TiO_2 nanocomposites under sunlight irradiation. Scientific Reports. 2024;14:84316. https://doi.org/10.1038/s41598-024-84316-0

Supporting Materials

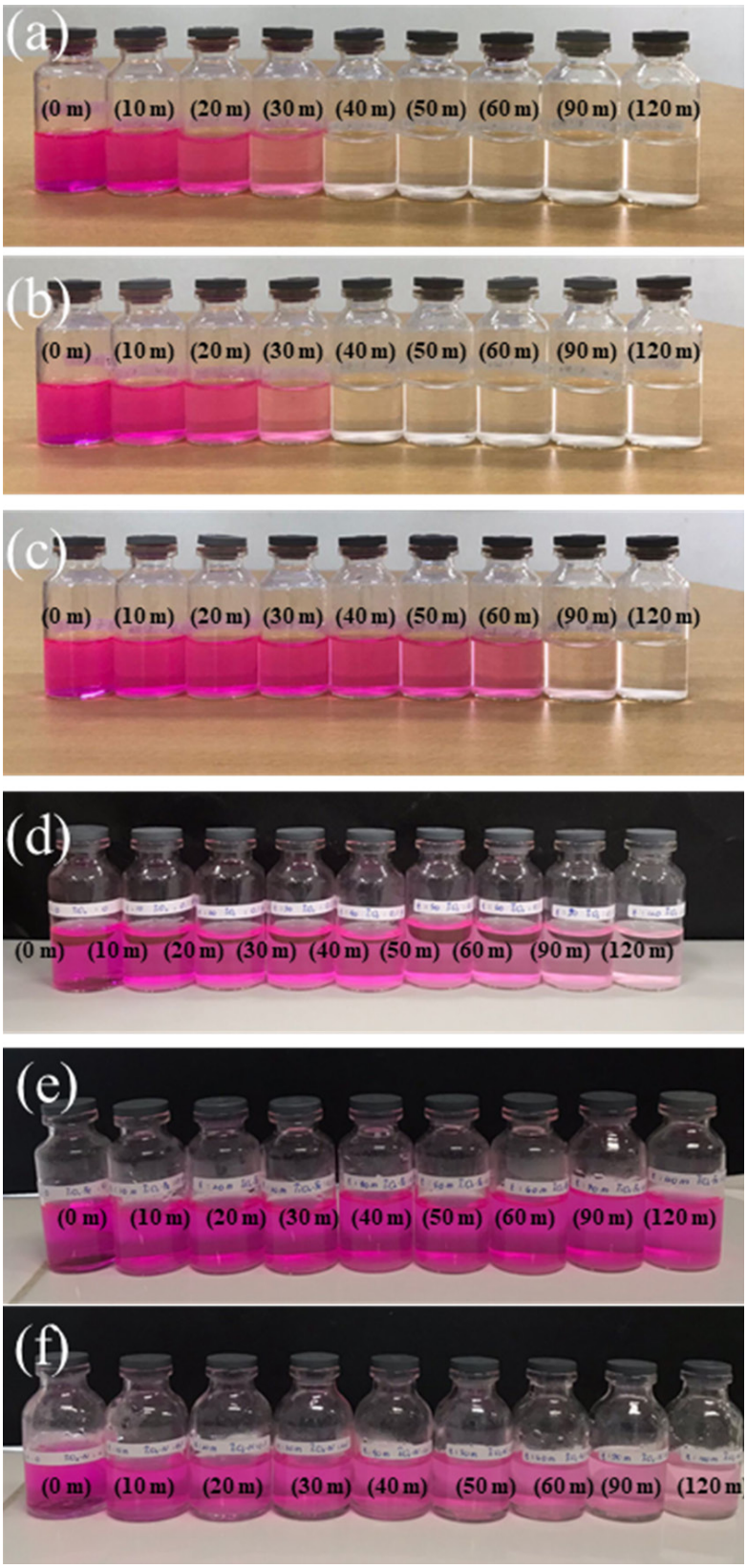

Supplemental Figure 1. Photocatalytic degradation of Rhodamine B using different catalysts under UV and visible light irradiation. (a) TiO_2 under UV light, (b) Fe-doped TiO_2 (Fe:TiO_2) under UV light, (c) N-doped TiO_2 (N:TiO_2) under UV light, (d) TiO_2 under visible light, (e) Fe:TiO_2 under visible light, and (f) N:TiO_2 under visible light.